5-kW, 96.5% Efficiency Capacitive Power Transfer System With a Five-Plate Coupler: Design and Optimization

Enguo Rong, *Graduate Student Member, IEEE*, Pan Sun, Gang Yang, Jinglin Xia, *Member, IEEE*, Zhe Liu, *Member, IEEE*, and Siqi Li, *Member, IEEE*

***Abstract*—Capacitive power transfer (CPT) has garnered significant interest in recent years, driven by efforts to enhance power and efficiency. This article presents advancements in CPT technology, focusing on the design of a novel five-plate coupler and the optimization of CPT systems. The proposed five-plate coupler features single-side shielding, which aims to simplify design complexity and reduce costs while maintaining performance. This study characterizes the five-plate coupler and compares its performance to traditional even-numbered plate configurations, highlighting the differences between odd and even plate designs and the unique characteristics of asymmetric couplers. In addition, the factors influencing efficiency are investigated, and an optimization method for CPT systems with asymmetric couplers is proposed to enhance the overall system performance. Experimental validation includes the development of a 5-kW prototype CPT system with a 100 mm airgap, achieving an impressive efficiency of 96.5%. These findings underscore the potential of the proposed design and optimization approach to set new benchmarks for CPT systems, facilitating their broader application in high-power scenarios.**

***Index Terms*—Capacitive power transfer (CPT), efficiency optimization, electric ships, five plates, reactive power.**

I. Introduction

WIRELESS power transfer (WPT) technology, known for its safety, intelligence, and convenience, finds extensive applications in fields such as electric vehicles [1], [2], rail transportation [3], electric ships [4], drones [5], [6], underwater vehicles [7], [8], and biomedical devices [9]. In recent years, WPT has undergone significant advancements, emerging as a prominent area of research [10].

Capacitive power transfer (CPT) represents a critical branch of WPT technology. It operates by utilizing capacitive coupling through high-frequency electric fields to generate displacement currents in the dielectric, thereby transferring power. Compared to other technologies, CPT offers advantages such as light-weight, cost-effectiveness, and reduced susceptibility to metallic foreign objects [11], [12], [13], [14], [15]. Initially constrained by the low permittivity of air, early CPT implementations were considered capable only of transmitting small powers over distances of a few millimeters. However, through years of development, CPT has demonstrated capabilities for effective transmission over distances around 100 mm, achieving power levels in the kilowatt range with efficiencies exceeding 90%. This makes it viable for high-power charging applications such as electric vehicles and electric ships.

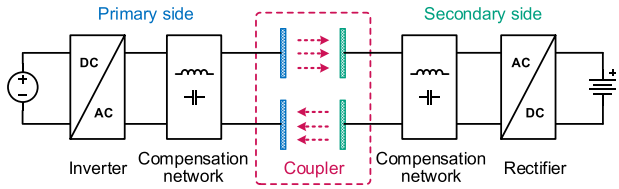

Fig. 1. Architecture of a typical CPT system.

Fig. 1 illustrates a typical CPT system comprising an inverter, compensation network, coupler, and rectifier. Among these, the coupler plays a pivotal role in power transfer. Previous studies have proposed various coupler designs, as depicted in Fig. 2. These include single-capacitor couplers with two plates [16], [17], as well as four-plate configurations, which can be horizontal [18], [19] or vertical [20], [21]. To mitigate outward electric field radiation, designs such as the six-plate structure [4], [22] and interleaved structure [23] have been introduced. Furthermore, multiple-input or multiple-output configurations [24], [25] have been devised for multichannel, multiload, or dynamic CPT applications. Relay-plate structures [26], [27] have also been explored for long-distance transfer.

While numerous coupler types cater to diverse applications, two considerations warrant further investigation. First, while the four-plate horizontal coupler is widely studied for its simplicity, it faces issues with electric field radiation and external

Received 3 July 2024; revised 17 August 2024; accepted 7 September 2024. Date of publication 18 September 2024; date of current version 12 December 2024. This work was supported in part by the National Key Research and Development Program of China under Grant 2022YFC3102800, in part by the National Natural Science Foundation of China under Grant 52007195, and in part by the Yunnan Fundamental Research Project under Grant 202301AT070429. Recommended for publication by Associate Editor X. Ruan. *(Corresponding authors: Pan Sun; Siqi Li.)*

Enguo Rong, Pan Sun, and Gang Yang are with the School of Electrical Engineering, Naval University of Engineering, Wuhan 430030, China (e-mail: 21100506@nue.edu.cn; 1007101026@nue.edu.cn; 1507111049@nue.edu.cn).

Jinglin Xia is with the Faculty of Mechanical and Electrical Engineering, Kunming University of Science and Technology, Kunming 650500, China (e-mail: xiajl22@kust.edu.cn).

Zhe Liu and Siqi Li are with the Department of Electrical Engineering, Kunming University of Science and Technology, Kunming 650500, China (e-mail: liuzhe0322@kust.edu.cn; lisiqi@kust.edu.cn).

Color versions of one or more figures in this article are available at https://doi.org/10.1109/TPEL.2024.3462410.

Digital Object Identifier 10.1109/TPEL.2024.3462410

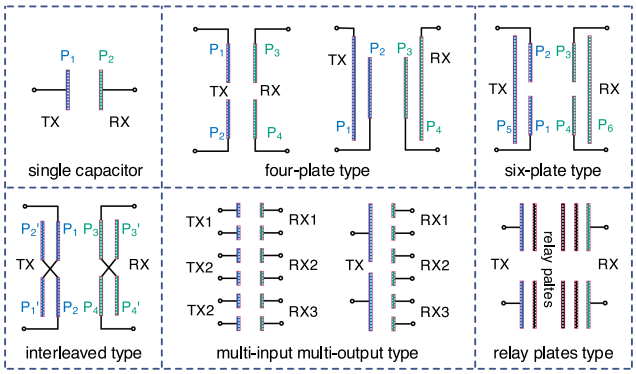

Fig. 2. Widely studied CPT coupler structures.

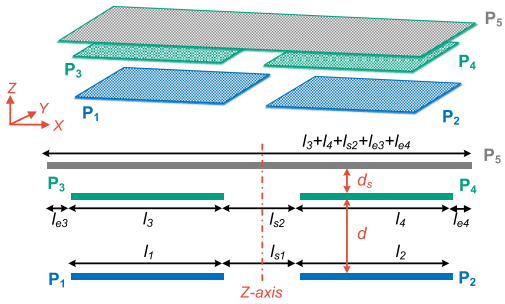

Fig. 3. Structure and dimensional definition of the five-plate coupler.

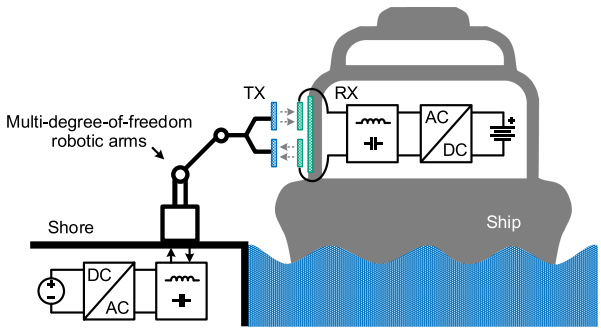

Fig. 4. Shore-to-ship CPT system based on a five-plate coupler.

parasitic capacitance. The six-plate design, with added shielding plates, addresses these issues but increases complexity. Thus, exploring the feasibility of a five-plate coupler, which provides single-sided shielding, could reduce design redundancy and lower costs. Second, existing structures typically use an even number of plates. It is essential to investigate couplers with an odd number of plates for single-sided shielding applications to discern differences from traditional designs.

In addition, as shown in Fig. 1, the CPT system includes compensation networks aimed at compensating reactive power within the system, thereby enhancing transfer power and efficiency. The research in [28] outlined a universal design approach for high-order compensation networks by applying constant voltage (CV)/constant current (CC) conditions on CPT. Wang et al. [29] summarized 144 feasible compensation network configurations based on zero-phase angle and load-independent output characteristics, further recommending 10 configurations. By utilizing a controlled voltage source (CVS) model of the coupler, the study in [30] proposed a universal design method for compensation networks, summarizing all the structures up to fourth order. Based on previous research, high-order compensation networks are crucial for high-power transfer, although their numerous parameters and high degrees of freedom complicate efficiency optimization.

Efforts have been made in previous studies to enhance the efficiency of high-power transfer in CPT systems. In [31], it was demonstrated that coupling coefficient significantly impacts efficiency. Achieving an 88% dc–dc efficiency was possible by increasing this coefficient, with an efficiency reaching 95% without rectifiers. In [32], both the coupler and compensation network were considered, along with the analysis of the inverter and rectifier effects, resulting in a 93% dc–dc efficiency. In addition, the authors in [12], [20], [22], [28], and [33] also highlighted research achieving over 90% dc–dc efficiency at kilowatt levels. In [34], a parallel compensating network was adopted, and by ensuring a 90° phase difference between voltages on both sides of the coupler, the system's dc–dc efficiency was improved to 94.5%. In [35], a two-stage optimization approach was proposed. The first stage optimized reactive power in the coupling capacitance, concluding that primary and secondary side parameters should be symmetrical. The second stage optimized reactive power across the entire system, achieving a dc–dc efficiency of 95.7%. This stands as the highest reported efficiency for CPT systems to date, validating the effectiveness of this method. However, this method is not applicable to asymmetric couplers and does not meet optimization conditions with single-sided shielding.

This study builds upon the five-plate coupler concept and reveals additional potential for efficiency improvements beyond those achieved in [35]. The efficiency optimization for asymmetric couplers, as opposed to symmetric structures, demonstrates broader applicability. By employing the proposed optimization method, asymmetric couplers have also been shown to achieve high-power, high-efficiency transfer. To substantiate these findings, a 5-kW CPT system prototype was implemented, achieving over 96.5% efficiency. Thus, this work elevates the power and efficiency of CPT systems to a higher standard, contributing to the practical advancement of CPT technology.

II. Structure and Characteristics of the Five-Plate Coupler

A. Plate Structure

As shown in Fig. 3, the five-plate coupler consists of four power transfer plates P_1–P_4 and one shielding plate P_5. Plates P_1 and P_2 are connected to the transmitting side, while P_3 and P_4 are connected to the receiving side. Plate P_5 remains unconnected. Typically, the shielding plate is positioned on the receiving side to meet stricter volume requirements and minimize the electric field safety limit. For instance, Fig. 4 illustrates a shore-to-ship CPT system employing the five-plate coupler. Due to the considerable distance between the ship and shore, there is ample space

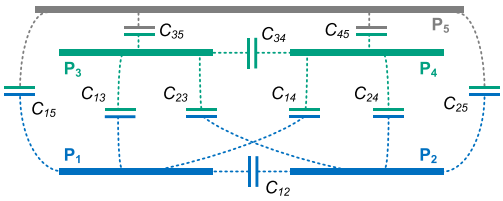

Fig. 5. Capacitance between any two plates.

on the primary side for extending the transmitter toward the ship via a manipulator, often obviating the need for shielding. Consequently, parasitic capacitance on the transmitter side is negligible. However, on the receiver side, the shielding plate creates multiple parasitic capacitances with the power transfer plates, affecting the equivalent capacitance and participating in the overall system resonance. Aside from Fig. 4, Appendix A presents further instances of single-side shielding scenarios, thereby expanding the versatility of the five-plate coupler.

To streamline the design, all four power transfer plates are square. As depicted in Fig. 3, their side lengths are defined as l_1–l_4. P_1 and P_2 lie in one plane with a separation of l_{s1}, while P_3 and P_4 lie in another plane with a separation of l_{s2}. The perpendicular distance from P_5 to the planes containing P_3 and P_4 is defined as the shielding distance d_s. The distance between the transmitting and receiving sides is defined as the transfer distance d. The distance from P_3 to the edge of P_5 is denoted as l_{e3}, and from P_4 to the edge of P_5 as l_{e4}. According to [22], electric field radiation arises from the electric field vector, which in turn is derived from the voltage difference. To achieve effective shielding, P_5 must completely cover the area of the power transfer plates, thereby confining the electric field vector from leaking out of the shielding plate side, irrespective of whether the opposite side is shielded. If high shielding requirements are necessary, increasing the size of the shielding plate is advisable.

B. Equivalent Circuit

As depicted in Fig. 5, each pair of plates forms a capacitor, resulting in a total of ten capacitors in the five-plate coupler. In comparison, previous studies have shown that a four-plate coupler forms 6 capacitors, while a six-plate coupler forms 15 capacitors. Zhang et al. simplified the full-capacitance model of four-plate [20] and six-plate [22] couplers using nodal voltage methods. A similar approach can be applied to the five-plate coupler [15]. However, a more refined design is proposed herein. Unlike traditional methods, applying symmetry conditions significantly simplifies the equivalent capacitance model. This design requires the coupler to be symmetric along the Z-axis. Specifically, P_1 and P_2 are of equal size, as are P_3 and P_4. There is no need for symmetry between the transmitting and receiving sides.

Fig. 6(a) illustrates the full-capacitance model of the five-plate coupler. Since P_5 is unconnected, there are only two ports: P_1 and P_2 serve as input ports, while P_3 and P_4 serve as output ports. The input voltage and current of the coupler are defined as $\boldsymbol{U}_{C1}$ and $\boldsymbol{I}_{C1}$, respectively, and the output voltage and current

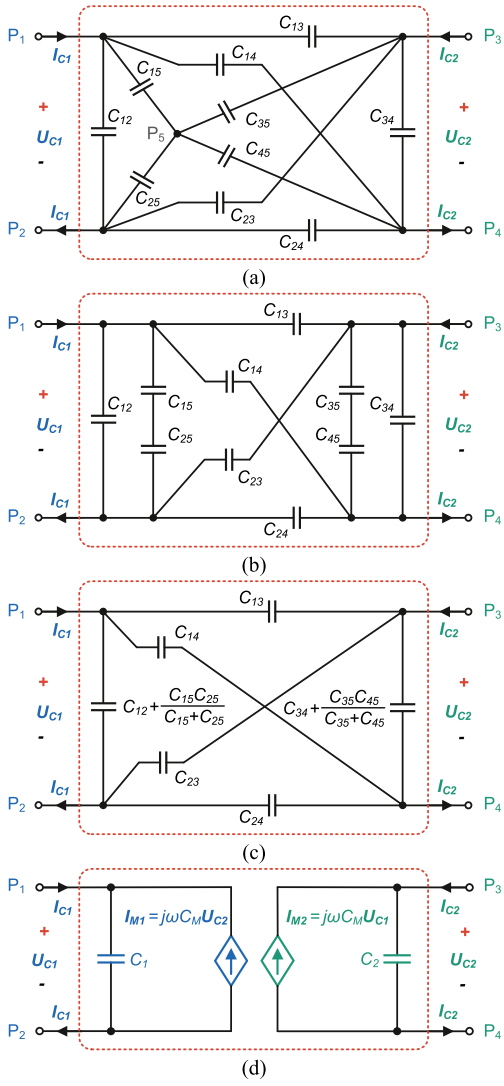

Fig. 6. Equivalent models of the five-plate coupler and their simplifications. (a) Full capacitance model. (b) Separation of P_5 based on symmetry. (c) Simplification based on series and parallel relationships. (d) CCS model.

as $\boldsymbol{U}_{C2}$ and $\boldsymbol{I}_{C2}$, respectively. Due to symmetry, $C_{15} = C_{25}$ and $C_{35} = C_{45}$. The points of connection for C_{15} and C_{25}, as well as C_{35} and C_{45}, are both at P_5 and are at zero potential. Consequently, the full-capacitance model is transformed into the configuration shown in Fig. 6(b). Subsequently, based on series and parallel relationships, C_{12}, C_{15}, and C_{25} are combined into one capacitance, while C_{24}, C_{35}, and C_{45} are combined into another, resulting in the six-capacitance model shown in Fig. 6(c). This model can further be transformed into the controlled current source (CCS) model depicted in Fig. 6(d).

In this study, vectors are denoted by bold italics, and scalars by italics. From Fig. 6(d), the following equations can be derived:

$$\begin{bmatrix} \boldsymbol{I}_{C1} \\ \boldsymbol{I}_{C2} \end{bmatrix} = \begin{bmatrix} j\omega C_1 & -j\omega C_M \\ -j\omega C_M & j\omega C_2 \end{bmatrix} \cdot \begin{bmatrix} \boldsymbol{U}_{C1} \\ \boldsymbol{U}_{C2} \end{bmatrix} \tag{1}$$

where C_1 represents the primary self-capacitance, C_2 represents the secondary self-capacitance, and C_M represents the mutual

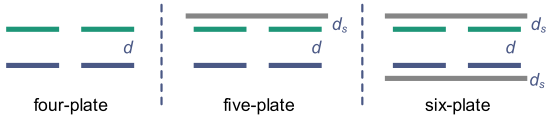

Fig. 7. Comparison of four-plate, five-plate, and six-plate couplers size.

TABLE I
DIMENSIONS OF THE COUPLER

Designator	Parameter	Value
l_1, l_2, l_3, l_4	Plate length	600 mm
l_{s1}, l_{s2}	Plate separation	100 mm
l_{l5}	Shielding plate length	1400 mm
l_{w5}	Shielding plate width	700 mm
l_{e3}, l_{e4}	Plate shielding edge	50 mm
d_s	Shielding distance	50 mm
d	Transfer distance	100 mm

capacitance, defined as

$$\begin{cases} C_1 = C_{12} + \frac{C_{15}C_{25}}{C_{15}+C_{25}} + \frac{(C_{13}+C_{14})(C_{23}+C_{24})}{C_{13}+C_{14}+C_{23}+C_{24}} \\ C_2 = C_{34} + \frac{C_{35}C_{45}}{C_{35}+C_{45}} + \frac{(C_{13}+C_{23})(C_{14}+C_{24})}{C_{13}+C_{14}+C_{23}+C_{24}} \\ C_M = \frac{C_{13}C_{24}-C_{14}C_{23}}{C_{13}+C_{14}+C_{23}+C_{24}}. \end{cases} \tag{2}$$

The coupling coefficient k_C is defined as

$$k_C = \frac{C_M}{\sqrt{C_1 \cdot C_2}}. \tag{3}$$

Thus, the five-plate coupler can be described using C_1, C_2, C_M, and k_C.

C. Capacitance Characteristics Analysis

Considering edge effects, direct calculation of capacitance values using parallel plate capacitance formulas is impractical. Therefore, finite element analysis (FEA) is employed to determine capacitance values [20], [22], [33], [34], [35].

To investigate the capacitance characteristics of the five-plate coupler, a comparative analysis is conducted with traditional four-plate and six-plate couplers. As shown in Fig. 7, finite element models of four-plate, five-plate, and six-plate coupler structures are constructed using Maxwell software. The primary distinction among these couplers lies in the number of shielding plates, with other parameters kept consistent. Specifically, the sizes of the power transfer plates in the four/five/six plates structures are equal, and the transfer distance is identical. The shielding plate sizes for the five-plate and six-plate structures are also identical, maintaining consistent shielding distances, as detailed in Table I.

Based on FEA results, capacitance between any two plates can be obtained. The equivalent capacitance of the five-plate coupler is calculated using (2). The equivalent capacitances of the four-plate and six-plate couplers are derived according to methods detailed in [20] and [22], respectively. Their coupling coefficients are calculated using (3).

First, the transfer distance of the three couplers is varied from 25 to 175 mm, while keeping other parameters fixed as per Table I. The characteristics of the equivalent mutual capacitance C_M and equivalent self-capacitances C_1, C_2 as a function of transfer distance are shown in Figs. 8 and 9, respectively.

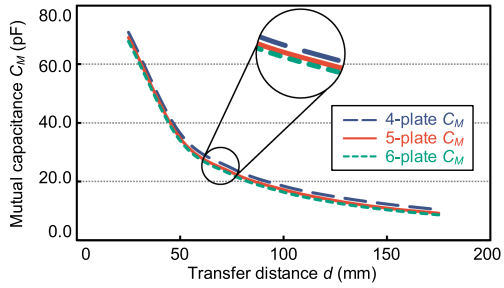

Fig. 8. Variation of mutual capacitance with transfer distance.

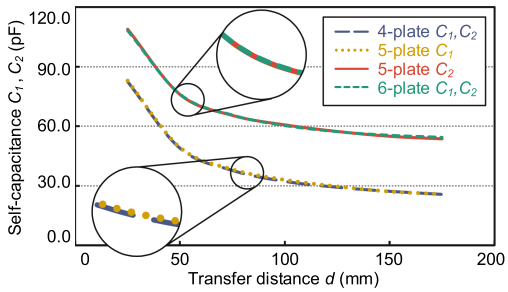

Fig. 9. Variation of self-capacitance with transfer distance.

According to Fig. 8, C_M decreases significantly as d increases for all three couplers. The C_M of the five-plate coupler is lower than that of the four-plate coupler but higher than that of the six-plate coupler. For $d = 100$ mm, C_M values are 18.40 pF, 17.23 pF, and 16.36 pF for the four-plate, five-plate, and six-plate couplers, respectively. Hence, shielding plates are observed to weaken coupling, and while more shielding plates enhance shielding effectiveness, they also correspondingly reduce coupling. Nevertheless, the differences are minor.

As shown in Fig. 9, the self-capacitances C_1 and C_2 decrease as d increases for all three couplers. The four-plate and six-plate structures exhibit symmetrical primary and secondary sides, resulting in $C_1 = C_2$. However, the presence of shielding plates significantly increases self-capacitance. Consequently, the self-capacitance of the six-plate coupler is markedly higher than that of the four-plate coupler. As for the five-plate coupler, being asymmetric in structure, $C_1 \neq C_2$. FEA results indicate that C_1 of the five-plate coupler is roughly equivalent to that of the four-plate coupler, and C_2 is comparable to that of the six-plate coupler. This indicates that shielding plates only affect self-capacitance on the same side, without impacting the opposing side.

The curves depicting the coupling coefficients as a function of d for the three couplers are shown in Fig. 10. Due to the decrease in C_M with increasing d, k_C decreases significantly. In addition, the substantial increase in self-capacitance due to shielding plates results in the lowest coupling coefficient for the six-plate coupler and the highest for the four-plate coupler, with

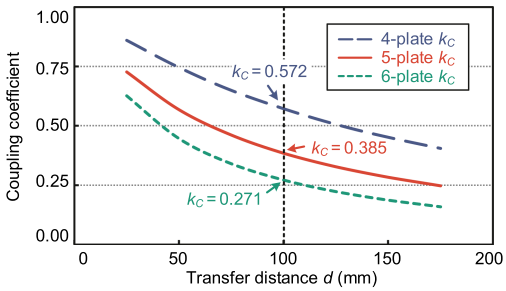

Fig. 10. Variation of coupling coefficient with transfer distance.

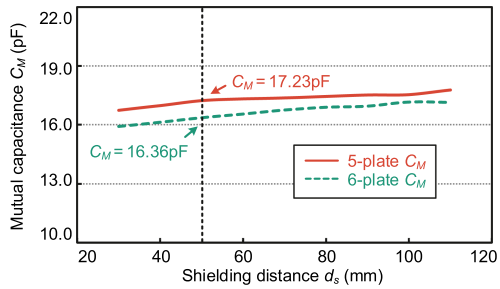

Fig. 11. Variation of mutual capacitance with shielding distance.

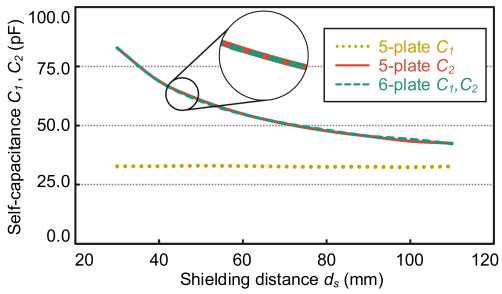

Fig. 12. Variation of self-capacitance with shielding distance.

the five-plate coupler positioned between them under the same transfer distance.

To further explore the influence of shielding plates, the transfer distance d is fixed at 100 mm, while the shielding distance d_s is varied from 30 to 110 mm. The variations in mutual capacitance and self-capacitance for the five-plate and six-plate couplers are illustrated in Figs. 11 and 12, respectively.

According to Fig. 11, C_M increases with d_s for both couplers, with minimal differences observed. Fig. 12 demonstrates that as d_s increases, C_1 and C_2 decrease for the six-plate coupler, while C_1 remains unchanged for the five-plate coupler. This confirms that shielding plates only affect self-capacitance on the same side, leaving the self-capacitance on the unshielded side unaffected.

The curves depicting the coupling coefficients as a function of d_s for the two couplers are shown in Fig. 13. As d_s increases, the decrease in self-capacitance leads to an increase in k_C. Notably, due to the variation in only C_2 for the five-plate coupler, its k_C exhibits smaller changes compared to the six-plate coupler.

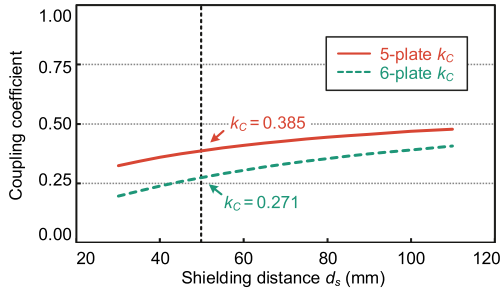

Fig. 13. Variation of coupling coefficient with shielding distance.

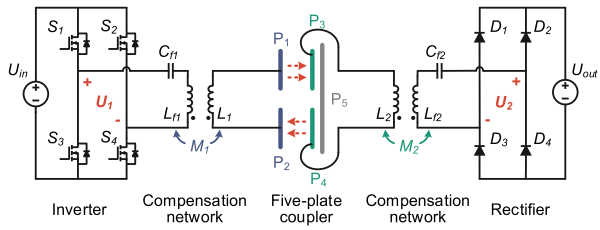

Fig. 14. Architecture of the proposed CPT system.

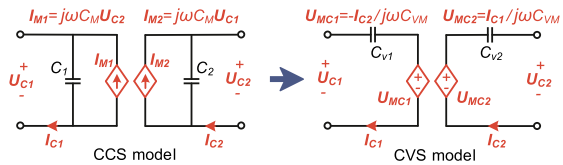

Fig. 15. Conversion of CCS into CVS model.

Combining Figs. 10 and 13, to maintain a higher coupling coefficient for the five-plate coupler, the transfer distance should not be too great, and the shielding distance should not be too close.

III. Compensation Network Design and Efficiency Optimization

A. Structure and Characteristics of the Compensation Network

While previous works have proposed various compensation networks, higher order compensation networks are necessary for achieving high-power transfer. This study investigates a 5-kW CPT system as an example. An *M-M* compensation network is selected, as shown in Fig. 14. Unlike double-sided *LCL* and double-sided *CLL* networks, it exhibits coupled inductors, implying higher integration and fewer components, while providing additional isolation.

In this system, depicted in Fig. 14, there are two pairs of coupled inductors and one capacitive coupler. Typically, coupled inductors are equivalently modeled using CVS. Capacitive coupler is represented by CCS model. For consistency in subsequent analysis, however, capacitive coupler is transformed into CVS model. This ensures uniform circuit models for coupled inductors and capacitive coupler, thereby simplifying analysis.

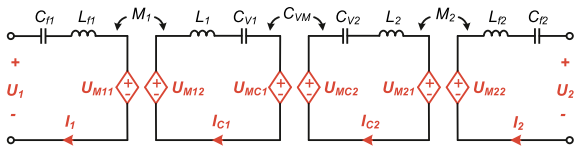

Fig. 16. Equivalent circuit of the system.

Based on Fig. 15, voltage–current equations for CCS and CVS models are separately derived

$$\begin{bmatrix} \boldsymbol{I_{C1}} \\ -\boldsymbol{I_{C2}} \end{bmatrix} = \begin{bmatrix} j\omega C_1 & -j\omega C_M \\ -j\omega C_M & j\omega C_2 \end{bmatrix} \cdot \begin{bmatrix} \boldsymbol{U_{C1}} \\ \boldsymbol{U_{C2}} \end{bmatrix} \tag{4}$$

$$\begin{bmatrix} \boldsymbol{U_{C1}} \\ \boldsymbol{U_{C2}} \end{bmatrix} = \begin{bmatrix} \frac{1}{j\omega C_{V1}} & \frac{1}{j\omega C_{VM}} \\ \frac{1}{j\omega C_{VM}} & \frac{1}{j\omega C_{V2}} \end{bmatrix} \cdot \begin{bmatrix} \boldsymbol{I_{C1}} \\ -\boldsymbol{I_{C2}} \end{bmatrix}. \tag{5}$$

Combining (4) and (5) yields

$$\begin{cases} C_{V1} = \frac{C_1C_2-C_M^2}{C_2} \\ C_{V2} = \frac{C_1C_2-C_M^2}{C_1} \\ C_{VM} = \frac{C_1C_2-C_M^2}{C_M}. \end{cases} \tag{6}$$

Thus, the system's equivalent circuit described by CVS is shown in Fig. 16. Series resonance conditions are adopted, enabling resonance relationships to be described as

$$\begin{aligned} \omega = 2\pi f &= \frac{1}{\sqrt{L_{f1}C_{f1}}} = \frac{1}{\sqrt{L_{f2}C_{f2}}} \\ &= \frac{1}{\sqrt{L_1 \cdot \frac{C_1C_2-C_M^2}{C_2}}} = \frac{1}{\sqrt{L_2 \cdot \frac{C_1C_2-C_M^2}{C_1}}}. \end{aligned} \tag{7}$$

According to Kirchhoff's voltage law, the circuit in Fig. 16 is represented as

$$\begin{cases} \boldsymbol{U_1} = \left(j\omega L_{f1} + \frac{1}{j\omega C_{f1}}\right)\boldsymbol{I_1} + \boldsymbol{U_{M11}} \\ \boldsymbol{U_{M12}} = \left(j\omega L_1 + \frac{C_2}{j\omega\left(C_1C_2-C_M^2\right)}\right)\boldsymbol{I_{C1}} + \boldsymbol{U_{MC1}} \\ \boldsymbol{U_{MC2}} = \left(j\omega L_2 + \frac{C_1}{j\omega\left(C_1C_2-C_M^2\right)}\right)\boldsymbol{I_{C2}} + \boldsymbol{U_{M21}} \\ \boldsymbol{U_{M22}} = \left(j\omega L_{f2} + \frac{1}{j\omega C_{f2}}\right)\boldsymbol{I_2} + \boldsymbol{U_2} \end{cases} \tag{8}$$

where

$$\begin{cases} \boldsymbol{U_{M11}} = -j\omega M_1\boldsymbol{I_{C1}} \\ \boldsymbol{U_{M12}} = j\omega M_1\boldsymbol{I_1} \\ \boldsymbol{U_{M21}} = -j\omega M_2\boldsymbol{I_2} \\ \boldsymbol{U_{M22}} = j\omega M_2\boldsymbol{I_{C2}} \\ \boldsymbol{U_{MC1}} = -\frac{C_M\boldsymbol{I_{C2}}}{j\omega\left(C_1C_2-C_M^2\right)} \\ \boldsymbol{U_{MC2}} = \frac{C_M\boldsymbol{I_{C1}}}{j\omega\left(C_1C_2-C_M^2\right)}. \end{cases} \tag{9}$$

Combining (7)–(9) allows solving for each mesh current as

$$\begin{cases} \boldsymbol{I_1} = \frac{C_M\boldsymbol{U_2}}{j\omega^3M_1M_2\left(C_1C_2-C_M^2\right)} \\ \boldsymbol{I_{C1}} = \frac{j\boldsymbol{U_1}}{\omega M_1} \\ \boldsymbol{I_{C2}} = \frac{\boldsymbol{U_2}}{j\omega M_2} \\ \boldsymbol{I_2} = \frac{jC_M\boldsymbol{U_1}}{\omega^3M_1M_2\left(C_1C_2-C_M^2\right)}. \end{cases} \tag{10}$$

According to (10), the system's transferred power is expressed as

$$P = \frac{U_1U_2C_M}{\omega^3M_1M_2\left(C_1C_2-C_M^2\right)}. \tag{11}$$

B. Efficiency Analysis

From Figs. 14 and 16, losses in the CPT system originate from inverters, rectifiers, inductors, and capacitors, defined respectively as $P_{\text{loss,inv}}$, $P_{\text{loss,rec}}$, $P_{\text{loss},L}$, and $P_{\text{loss},C}$. Therefore, efficiency is expressed as

$$\eta = \frac{P}{P + P_{\text{loss,inv}} + P_{\text{loss,rec}} + P_{\text{loss},L} + P_{\text{loss},C}} \tag{12}$$

where $P_{\text{loss},L}$ and $P_{\text{loss},C}$ are defined as

$$\begin{cases} P_{\text{loss},L} = P_{\text{loss},Lf1} + P_{\text{loss},Lf2} + P_{\text{loss},L1} + P_{\text{loss},L2} \\ P_{\text{loss},C} = P_{\text{loss},Cf1} + P_{\text{loss},Cf2} + P_{\text{loss},CV1} + P_{\text{loss},CV2}. \end{cases} \tag{13}$$

Defining the quality factor of each inductance and capacitance as their reactive power to active power ratio, their losses can be expressed as

$$\begin{cases} P_{\text{loss},Lf1} = \frac{Q_{Lf1}}{Q_{Lf1}^*}, \quad P_{\text{loss},Lf2} = \frac{Q_{Lf2}}{Q_{Lf2}^*}, \quad P_{\text{loss},L1} = \frac{Q_{L1}}{Q_{L1}^*}, \\ \qquad P_{\text{loss},L2} = \frac{Q_{L2}}{Q_{L2}^*} \\ P_{\text{loss},Cf1} = \frac{Q_{Cf1}}{Q_{Cf1}^*}, \quad P_{\text{loss},Cf2} = \frac{Q_{Cf2}}{Q_{Cf2}^*}, \quad P_{\text{loss},CV1} = \frac{Q_{CV1}}{Q_{CV1}^*}, \\ \qquad P_{\text{loss},CV2} = \frac{Q_{CV2}}{Q_{CV2}^*} \end{cases} \tag{14}$$

where, Q_{Lf1}, Q_{Lf2}, Q_{L1}, Q_{L2}, Q_{Cf1}, Q_{Cf2}, Q_{CV1}, and Q_{CV2} represent the reactive power of each inductance and capacitance. $Q_{Lf1}{}^*$, $Q_{Lf2}{}^*$, $Q_{L1}{}^*$, $Q_{L2}{}^*$, $Q_{Cf1}{}^*$, $Q_{Cf2}{}^*$, $Q_{CV1}{}^*$, and $Q_{CV2}{}^*$ denote their quality factors.

Thus, (13) transforms into

$$\begin{cases} P_{\text{loss},L} = \frac{Q_{Lf1}}{Q_{Lf1}^*} + \frac{Q_{Lf2}}{Q_{Lf2}^*} + \frac{Q_{L1}}{Q_{L1}^*} + \frac{Q_{L2}}{Q_{L2}^*} \\ P_{\text{loss},C} = \frac{Q_{Cf1}}{Q_{Cf1}^*} + \frac{Q_{Cf2}}{Q_{Cf2}^*} + \frac{Q_{CV1}}{Q_{CV1}^*} + \frac{Q_{CV2}}{Q_{CV2}^*} \end{cases} \tag{15}$$

where Q_L sums all inductors' reactive powers and Q_C sums all capacitors' reactive powers, i.e.,

$$\begin{cases} Q_L = Q_{Lf1} + Q_{Lf2} + Q_{L1} + Q_{L2} \\ Q_C = Q_{Cf1} + Q_{Cf2} + Q_{CV1} + Q_{CV2}. \end{cases} \tag{16}$$

Assuming equal quality factors for all inductors and capacitors

$$\begin{cases} Q_L^* = Q_{Lf1}^* = Q_{Lf2}^* = Q_{L1}^* = Q_{L2}^* \\ Q_C^* = Q_{Cf1}^* = Q_{Cf2}^* = Q_{CV1}^* = Q_{CV2}^* \end{cases} \tag{17}$$

efficiency can then be further expressed as

$$\eta = \frac{1}{1 + \frac{P_{\text{loss,inv}}}{P} + \frac{P_{\text{loss,rec}}}{P} + \frac{Q_L}{Q_L^* P} + \frac{Q_C}{Q_C^* P}}. \tag{18}$$

According to (18), three measures can enhance system efficiency. First, reducing losses in inverters and rectifiers by selecting MOSFET and diode devices with low conduction and switching losses. Second, enhancing inductor and capacitor quality factors $Q_L{}^*$ and $Q_C{}^*$. This involves choosing devices with low losses and minimizing ac resistance during component manufacture. Third, reducing the ratio of reactive power to active power for inductance and capacitance. The optimization goal defined in this study is to minimize Q_L/P and Q_C/P.

C. Reactive Power Optimization

According to Fig. 16, since inductance and capacitance employ the same model, the same method can be utilized to calculate their reactive power. The reactive power of all inductors and capacitors in the system is expressed as follows:

$$Q_{Lf1} = I_1^2 \omega L_{f1} = \frac{L_{f1} C_M^2 U_2^2}{\omega^5 M_1^2 M_2^2 (C_1 C_2 - C_M^2)^2} \tag{19}$$

$$Q_{Lf2} = I_2^2 \omega L_{f2} = \frac{L_{f2} C_M^2 U_1^2}{\omega^5 M_1^2 M_2^2 (C_1 C_2 - C_M^2)^2} \tag{20}$$

$$Q_{L1} = I_{C1}^2 \omega L_1 = \frac{L_1 U_1^2}{\omega M_1^2} \tag{21}$$

$$Q_{L2} = I_{C2}^2 \omega L_2 = \frac{L_2 U_2^2}{\omega M_2^2} \tag{22}$$

$$Q_{Cf1} = \frac{I_1^2}{\omega C_{f1}} = \frac{C_M^2 U_2^2}{\omega^7 M_1^2 M_2^2 C_{f1} (C_1 C_2 - C_M^2)^2} \tag{23}$$

$$Q_{Cf2} = \frac{I_2^2}{\omega C_{f2}} = \frac{C_M^2 U_1^2}{\omega^7 M_1^2 M_2^2 C_{f2} (C_1 C_2 - C_M^2)^2} \tag{24}$$

$$Q_{CV1} = \frac{I_{C1}^2}{\omega C_{V1}} = \frac{C_2 U_1^2}{\omega^3 M_1^2 (C_1 C_2 - C_M^2)} \tag{25}$$

$$Q_{CV2} = \frac{I_{C2}^2}{\omega C_{V2}} = \frac{C_1 U_2^2}{\omega^3 M_2^2 (C_1 C_2 - C_M^2)}. \tag{26}$$

The two inductive coupling coefficients of the compensation network are defined as k_{L1} and k_{L2}, represented as

$$\begin{cases} k_{L1} = \frac{M_1}{\sqrt{L_1 \cdot L_{f1}}} \\ k_{L2} = \frac{M_2}{\sqrt{L_2 \cdot L_{f2}}}. \end{cases} \tag{27}$$

Therefore, based on (7), (16), and (27), Q_L can be represented as

$$Q_L = \frac{\omega C_{f1} C_M^2 U_1^2 + \omega C_{f2} C_M^2 U_2^2}{k_{L1}^2 k_{L2}^2 C_1 C_2} + \frac{\omega C_{f1} U_1^2}{k_{L1}^2} + \frac{\omega C_{f2} U_2^2}{k_{L2}^2}. \tag{28}$$

Q_C can be represented as

$$Q_C = \frac{\omega C_{f1} C_M^2 U_1^2 + \omega C_{f2} C_M^2 U_2^2}{k_{L1}^2 k_{L2}^2 C_1 C_2} + \frac{\omega C_{f1} U_1^2}{k_{L1}^2} + \frac{\omega C_{f2} U_2^2}{k_{L2}^2}. \tag{29}$$

This indicates that the inductive reactive power and capacitive reactive power in the system are equal. The transfer reactive power Q can be defined as

$$Q = Q_L = Q_C. \tag{30}$$

Thus, combining (3), (11), and (27)–(30), the ratio of transfer reactive power to transfer active power can be calculated as

$$\begin{aligned} \frac{Q}{P} &= \frac{\sqrt{C_{f1}} \left(k_{L2}^2 + k_C^2\right)}{k_{L1} k_{L2} k_C} \frac{U_1}{U_2} + \frac{\sqrt{C_{f2}} \left(k_{L1}^2 + k_C^2\right)}{k_{L1} k_{L2} k_C} \frac{U_2}{U_1} \\ &\geqslant 2 \sqrt{\frac{1}{k_C^2} + \frac{k_C^2}{k_{L1}^2 k_{L2}^2} + \frac{k_{L1}^2 + k_{L2}^2}{k_{L1}^2 k_{L2}^2}} \end{aligned} \tag{31}$$

where the inequality holds under the following conditions:

$$\frac{U_1}{U_2} = \frac{\sqrt{C_{f2}} \left(k_{L1}^2 + k_C^2\right)}{\sqrt{C_{f1}} \left(k_{L2}^2 + k_C^2\right)}. \tag{32}$$

Defining A and B as

$$\begin{cases} A = \frac{1}{k_C^2} + \frac{k_C^2}{k_{L1}^2 k_{L2}^2} \\ B = \frac{k_{L1}^2 + k_{L2}^2}{k_{L1}^2 k_{L2}^2}. \end{cases} \tag{33}$$

Then (31) can be expressed as

$$\frac{Q}{P} \geqslant 2\sqrt{A + B}. \tag{34}$$

A achieves its minimum value as

$$A \geqslant 2 \sqrt{\frac{1}{k_{L1}^2 k_{L2}^2}} = \frac{2}{k_{L1} k_{L2}}. \tag{35}$$

Satisfying condition (35) requires

$$k_C^2 = k_{L1} k_{L2}. \tag{36}$$

B achieves its minimum value as

$$B \geqslant \frac{2 k_{L1} k_{L2}}{k_{L1}^2 k_{L2}^2} = \frac{2}{k_{L1} k_{L2}}. \tag{37}$$

Satisfying condition (37) requires

$$k_{L1} = k_{L2}. \tag{38}$$

When both conditions (36) and (38) are simultaneously satisfied, substituting (35) and (37) into (34) yields the minimum value of Q/P as

$$\frac{Q}{P} = \frac{4}{\sqrt{k_{L1} k_{L2}}} = \frac{4}{k_C}. \tag{39}$$

If only condition (36) is satisfied and not (38), the minimum value of Q/P is

$$\frac{Q}{P} = 2 \sqrt{\frac{2}{k_{L1} k_{L2}} + \frac{1}{k_{L1}^2} + \frac{1}{k_{L2}^2}} = 2 \left(\frac{1}{k_{L1}} + \frac{k_{L1}}{k_C^2} \right). \tag{40}$$

If only condition (38) is satisfied and not (36), the minimum value of Q/P is

$$\frac{Q}{P} = 2 \sqrt{\frac{2}{k_{L1} k_{L2}} + \frac{1}{k_C^2} + \frac{k_C^2}{k_{L1}^2 k_{L2}^2}} = 2 \sqrt{\frac{2}{k_{L1}^2} + \frac{1}{k_C^2} + \frac{k_C^2}{k_{L1}^4}}. \tag{41}$$

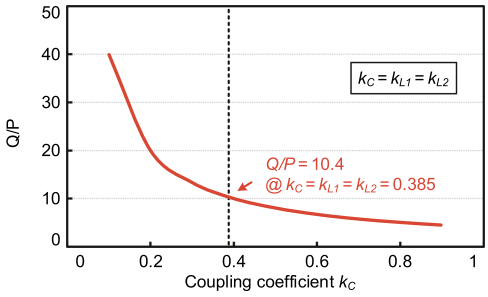

Fig. 17. Variation of Q/P when conditions (36) and (38) are satisfied simultaneously.

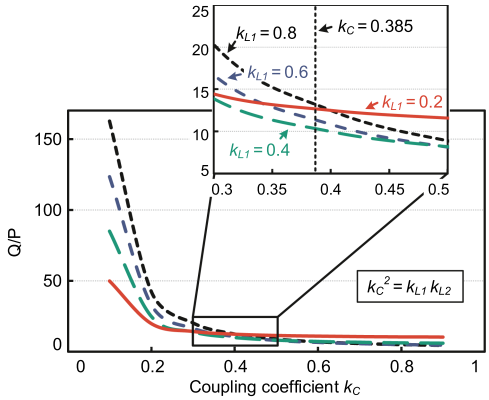

Fig. 18. Variation of Q/P when only condition (36) is satisfied.

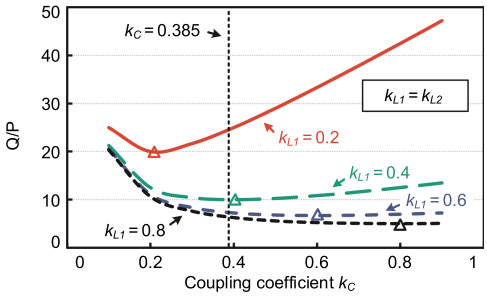

Fig. 19. Variation of Q/P when only condition (38) is satisfied.

It is noteworthy that while (39) provides the theoretical minimum value of *Q/P*, for a specific coupler, *Q/P* derived from this condition may not necessarily be the minimum. As shown in Fig. 17, when conditions (36) and (38) are satisfied simultaneously, *Q/P* significantly decreases with increasing k_C, consistent with theoretical analysis. However, k_C cannot increase indefinitely. Based on Figs. 10 and 13, and corresponding analysis, when ensuring a certain transfer distance and constrained by the coupler's volume, k_C is limited by the transfer and shielding distances. For instance, at a transfer distance of 100 mm and a shielding distance of 50 mm, $k_C = 0.385$. Calculating *Q/P* via (39) results in 10.4.

Figs. 18 and 19, respectively, illustrate *Q/P* under conditions (36) and (38). When only condition (36) is satisfied, *A* achieves its minimum value, and *Q/P* is primarily influenced by *B*. According to (40), Fig. 18 is derived. At the same k_{L1}, larger k_C results in smaller *Q/P*. However, for a specific coupler such as in this design where $k_C = 0.385$, increasing k_{L1} initially increases then decreases *Q/P*.

To further reduce *Q/P*, consider satisfying condition (38) without satisfying condition (36). According to (41), *Q/P* is as shown in Fig. 19. Firstly, at the same k_{L1}, *Q/P* is minimized when $k_C = k_{L1}$, consistent with the result from (39). Secondly, at the same k_C, increasing k_{L1} reduces *Q/P*. Although *A* increases under these circumstances, *B* decreases more significantly, overall reducing *Q/P*.

In addition, according to Fig. 19, the reduction in *Q/P* becomes less significant after k_{L1} exceeds 0.4. However, as per (11) and (27), increasing k_{L1} significantly reduces power. Hence, caution is required when increasing k_{L1}. This design ultimately balances considerations and selects $k_{L1} = k_{L2} = 0.45$. Calculating via (41) yields *Q/P* as 9.0.

In summary, the parameter design condition recommended by this study is to satisfy both (32) and (38), which optimizes the efficiency of the CPT system. It can be observed that when both conditions are met, they can be expressed as follows:

$$\begin{cases} \dfrac{U_1}{U_2} = \dfrac{\sqrt{C_{f2}}}{\sqrt{C_{f1}}} \\ k_{L1} = k_{L2}. \end{cases} \tag{42}$$

This indicates that once the system's input and output voltages are determined, high efficiency can be achieved by adjusting the compensation network. If the input and output voltages are equal, then C_{f1} and C_{f2} should also be equal. With k_{L1} and k_{L2} are equal, the compensation network parameters are effectively symmetric. Moreover, according to Fig. 19, for a given k_{L1}, *Q/P* initially decreases and then increases with increasing k_C. Conversely, for a given k_C, *Q/P* decreases with increasing k_{L1}. Therefore, the efficiency optimization strategy should first maximize the coupling coefficient of the coupler and then improve the coupling coefficient of the compensation network. On the other hand, when k_{L1} and k_{L2} are sufficiently large, k_C variations within a wide range have minimal impact on *Q/P*, implying that the coupler influence can be mitigated by adjusting the external compensation network.

It is important to note that although the proposed five-plate coupler has asymmetric primary and secondary sides, the asymmetry only affects k_C during efficiency optimization. The proposed method achieves optimal efficiency by adjusting the compensation network parameters. Thus, this method is applicable to both symmetric and asymmetric couplers, overcoming the limitation of optimization methods relying on symmetric couplers as noted in [35]. Besides the five-plate coupler, Appendix B provides examples of other asymmetric couplers that can also be optimized using this method. Furthermore, this method is applicable to any compensation network, although specific optimization conditions and parameters will vary. The condition (42) is specific to the *M-M* compensation network used, which is easy to satisfy and implement. Therefore, the *M-M* compensation network is recommended as the optimal structure for the five-plate CPT system.

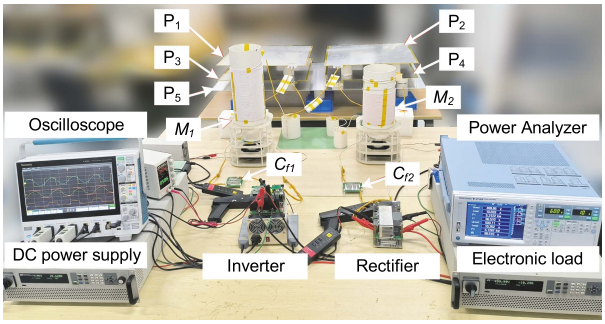

Fig. 20. Experimental setup.

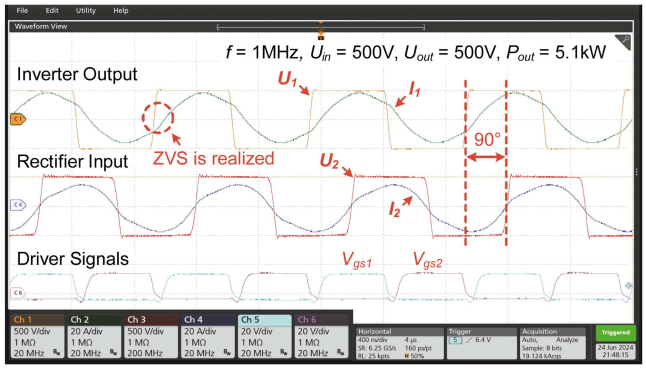

Fig. 21. Voltage and current waveforms from MSO46.

TABLE II
PARAMETERS OF THE CPT SYSTEMS

Designator	Parameter	Value
C_{f1}	Source-side capacitance	2.26 nF
C_{f2}	Load-side capacitance	2.2 nF
L_{f1}	Source-side inductance	11.4 μH
L_{f2}	Load-side inductance	11.4 μH
L_1	Primary-side inductance	901.2 μH
L_2	Secondary-side inductance	490.0 μH
k_{L1}	Primary inductive coupling coefficient	0.45
k_{L2}	Secondary inductive coupling coefficient	0.45
k_C	Capacitive coupling coefficient	0.385
C_1	Primary self-capacitance	33.0 pF
C_2	Secondary self-capacitance	60.7 pF
C_M	Mutual capacitance	17.23 pF

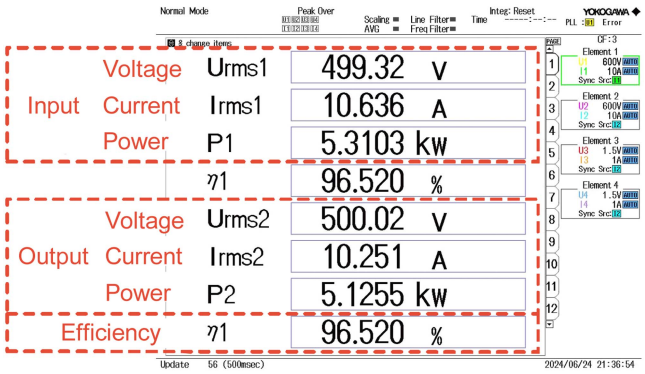

Fig. 22. Power and efficiency screenshots from WT1804E.

IV. EXPERIMENTAL VALIDATION

A. Experimental Setup

A 5-kW prototype was implemented to validate the proposed coupler and CPT system. The experimental setup, depicted in Fig. 20, was configured following the system structure shown in Fig. 14. The input to the system was provided by a dc power supply model IT6000D. The output was managed by an electronic load model IT6000C, configured in CV mode to simulate a high-voltage battery and provide adjustable voltage to emulate various load conditions and operating scenarios. The inverter utilized four IMZ120R045M1 silicon carbide (SiC) devices, with a TMS320F280049 control chip generating a 1 MHz control signal. The rectifier employed four C4D40120D SiC diodes. Voltage and current waveforms were measured using an MSO46 oscilloscope, while a WT1804E power analyzer measured power and efficiency.

A five-plate coupler prototype was constructed, with plates P_1–P_4 made of 600 mm×600 mm×2 mm aluminum and P_5 of a single 1400 mm×700 mm×2 mm aluminum plate. The transfer distance was set to 100 mm, and the shielding distance to 50 mm, adjusted using PVC tubing.

The target output power was 5 kW, with $U_{\text{in}} = U_{\text{out}} = 500$ V and $f = 1$ MHz as the rated operating conditions. Compensation network parameters were calculated according to (7) and (11), as given in Table II. The inductors were wound with AWG46 Litz wire: L_{f1} and L_{f2} were specified as 0.04 mm × 4500 strands due to their high current, while L_1 and L_2 were specified as 0.04 mm×2000 strands for their relatively lower current. Capacitors made of C0G material were connected in series and parallel to enhance voltage and current tolerance. To achieve zero voltage switching (ZVS) for MOSFETs, C_{f1} was slightly larger than C_{f2} to present a weakly inductive input impedance.

B. Experimental Results

Under rated operating conditions, inverter output voltage and current, rectifier input voltage and current, and drive signal waveforms are shown in Fig. 21. The waveforms demonstrate a well-established resonance state, with $\boldsymbol{I_1}$ slightly lagging $\boldsymbol{U_1}$, indicating ZVS achievement. $\boldsymbol{I_2}$ lags $\boldsymbol{U_1}$ by 90°, consistent with analysis in (10). According to Fig. 22, the output power reached 5.1 kW, with a dc–dc efficiency of 96.52%.

Next, system efficiency was tested under load conditions of $U_{\text{out}} = 500$ V, 400 V, and 300 V, as shown in Fig. 23. For each load condition, U_{in} ranged from 100 to 500 V in 50 V increments. According to Fig. 23, power increases with U_{in} and U_{out}, consistent with analysis in (11). The maximum power points under all three load conditions occurred at $U_{\text{in}} = 500$ V. At U_{out} of 500 V, 400 V, and 300 V, output power exceeded 5 kW, 4 kW, and 3 kW, respectively.

However, the points of maximum efficiency do not align with maximum power points under each load condition. Efficiency was 96.52% when $U_{\text{out}} = U_{\text{in}} = 500$ V, 96.27% when

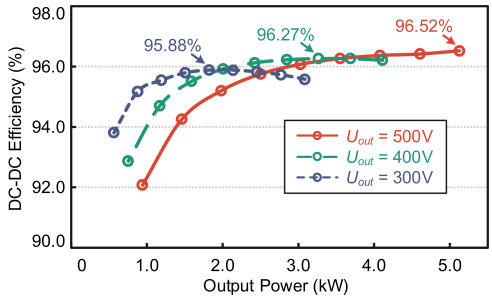

Fig. 23. Efficiency–power curves for different load conditions.

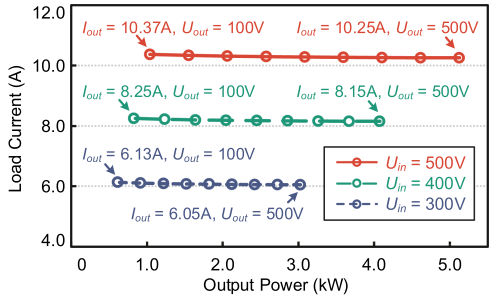

Fig. 24. Constant output current characteristics of the system.

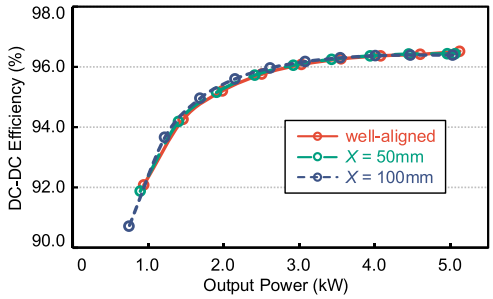

Fig. 25. *X*-direction offset performance.

$U_{\text{out}} = U_{\text{in}} = 400$ V, and 95.88% when $U_{\text{out}} = U_{\text{in}} = 300$ V, indicating maximum efficiency is achieved when U_{in} equals U_{out}, consistent with (42) analysis.

Subsequently, with U_{in} fixed at 500 V, 400 V, and 300 V, output current under varying loads was tested, as shown in Fig. 24. At the rated input voltage of $U_{\text{in}} = 500$ V, even with a 500% increase in load voltage, output current changed by only 1.16%. At U_{in} of 400 V and 300 V, output current changed by only 1.21% and 1.31%, respectively. Thus, the system demonstrates excellent CC characteristics, consistent with analysis in (10).

Performance with misaligned couplers was also tested. X and Y represent distances of coupler misalignment along the X and Y directions. As shown in Fig. 25, at $X = 100$ mm under rated operating conditions, output power decreased by 12.75%, with efficiency dropping to 96.39%. By increasing input voltage to 1.12× the rated voltage, a 5-kW output power can be maintained. As shown in Fig. 26, at $Y = 100$ mm under rated conditions, output power decreased by 5.34%, with efficiency

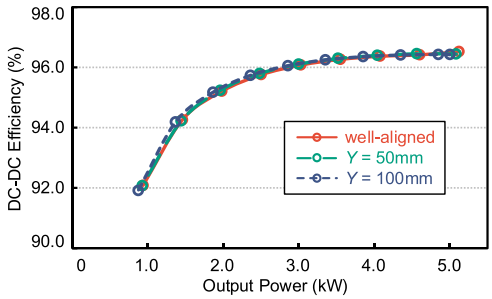

Fig. 26. *Y*-direction offset performance.

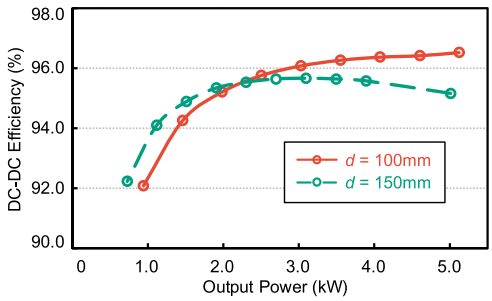

Fig. 27. *Z*-direction offset performance.

dropping to 96.43%. By increasing input voltage to 1.03× the rated voltage, a 5-kW output power can be maintained. These results demonstrate the system's misalignment tolerance, with better tolerance observed in the *Y*-direction.

In addition, the system was tested at different transfer distances, which also corresponds to the *Z*-direction misalignment. As shown in Fig. 27, for $d = 150$ mm, under rated conditions, the output power decreased by 24.05%, and the efficiency fell to 95.57%. Increasing the input voltage to 1.28× the rated value maintained the 5 kW output power. This result suggests that the system is more sensitive to the *Z*-direction misalignment. In applications depicted in Fig. 4, integrating the coupler into mechanical systems, such as mooring systems and multi-degree-of-freedom robotic arms, could help maintain a constant transfer distance and avoid significant impacts on system performance [36], [37].

From Fig. 22, the total system loss was calculated to be 184.8 W. Losses for the inductors, capacitors, inverter, and rectifier were determined based on models provided in [20] and [38]. Since the system achieved ZVS, the inverter was considered to have no turn-ON loss, with only conduction loss and turn-OFF loss being considered. The losses of the plates were obtained by subtracting the component losses from the total loss. The loss breakdown of the system is shown in Fig. 28. As shown, optimization has significantly reduced the losses in the compensation network and coupler compared to previous studies [4], [20], [22], [34], [35]. Conversely, inverter and rectifier losses now account for a larger portion. Future work could focus on improving the efficiency of megahertz-level inverters and using synchronous rectification techniques to enhance rectifier efficiency, thereby further increasing the overall system efficiency.

TABLE III
COMPARISON WITH STATE-OF-THE-ART HIGH-POWER CPT SYSTEMS

Publication time	Number of plates	Symmetrical or not*	Compensation network	Power (kW)	Frequency (MHz)	DC–DC efficiency	Distance (mm)	Coupling area (cm^2)	WPTFOM (W/m^2)
2015 [12]	4	Symmetric	*LCLC-LCLC*	2.4	1	90.8%	150	7442	61
2018 [22]	6	Symmetric	*LCL-LCL*	1.97	1	91.65%	150	7442	55
2020 [28]	4	Symmetric	*LCLC-LCLC*	1.5	1	93.57%	150	7442	55
2024 [33]	6	Asymmetric	*LCL-LCL*	6.06	1	92.3%	60	5124	129
2023 [34]	4	Asymmetric	*M-M*	3.55	2.5	94.2%	10	883	233
2022 [35]	6	Symmetric	*M-M*	3.0	1	95.7%	100	7200	114
This work	**5**	**Asymmetric**	***M-M***	**5.13**	**1**	**96.52%**	**100**	**7200**	**241**

* Note: Symmetrical means that the transmitter and receiver sides of the coupler have the same dimensions. The opposite is asymmetrical.

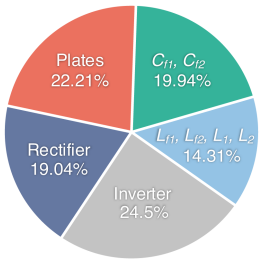

Fig. 28. Loss breakdown of the system.

C. Evaluation and Comparison

To evaluate the implemented system, the figure-of-merit for wireless power transfer (WPTFOM) was adopted [39], defined as

$$\text{WPTFOM} = \frac{P \cdot d}{(100 - \eta \cdot 100) \cdot S^{3/2}} \tag{43}$$

where P is the transferred power, d is the transfer distance, η is the dc–dc efficiency, and S is the coupling area.

According to (43), the calculated WPTFOM for this work is 241 W/m^2. This places the power density of the CPT systems rival to that of inductive power transfer systems [39].

This work also compares with recent advancements in kilowatt-level CPT systems, as summarized in Table III. Previous high-power CPT systems have predominantly utilized four-plate or six-plate couplers. For instance, Lu et al. [12] and Zhang et al. [22], respectively, mark the first prototypes to achieve kilowatt-level transfer using four-plate and six-plate couplers. In comparison, this study demonstrates that a five-plate coupler can also achieve high-power transfer, with a notable 5 kW output. While Kodeeswaran et al. [33] achieved 6 kW, slightly higher than this work, its efficiency and transfer distance were lower, resulting in a slightly lower WPTFOM.

Since 2020, CPT systems have seen efficiency break-throughs surpassing 93% [28], [34], [35], with concurrent advancements in power density, achieving a WPTFOM of 233 in kilowatt-level transfers [34]. Building upon these advancements, the current study further enhances both the efficiency and power density of CPT systems. Compared with state-of-the-art CPT systems under similar conditions of frequency, distance, and coupling area, this work achieves the highest dc–dc efficiency and WPTFOM. This confirms the high-efficiency and high-power-density characteristics of the implemented CPT system. It should be noted that this study employs a five-plate asymmetrical coupler to demonstrate high-efficiency performance. However, this does not imply that high efficiency is exclusive to asymmetrical designs. The proposed efficiency optimization methods are also applicable to traditional four-plate and six-plate couplers.

V. CONCLUSION

In conclusion, this article investigates the design and performance of a CPT system utilizing a novel five-plate coupler. First, it provides a detailed analysis of the equivalent circuit and capacitance characteristics of the five-plate coupler. Second, these characteristics are compared with those of traditional four-plate and six-plate couplers using FEA. Third, the transmission characteristics and efficiency of the CPT system, equipped with a five-plate coupler and an *M-M* compensation network, are analyzed. An efficiency optimization method suitable for asymmetrical couplers is proposed, which optimizes efficiency by adjusting the ratio of reactive to active power and tuning the compensation network parameters for optimal efficiency conditions. Finally, a 5-kW prototype was implemented and validated for analysis. At a 100-mm transfer distance, the system demonstrated favorable CC characteristics and misalignment tolerance. Notably, it achieved a high dc–dc efficiency of up to 96.5%. These results highlight the potential of the five-plate coupler to enhance the performance and applicability of CPT systems, particularly in high-power applications requiring efficiency and compact design.

APPENDIX A

This appendix explores additional applications for the five-plate coupler.

The five-plate coupler was originally introduced to provide single-side shielding, making it suitable for high-power transfer applications, such as electric vehicles, electric ships, and industrial robots. Traditional four-plate CPT couplers generate strong electric field radiation during high-power transfer. While

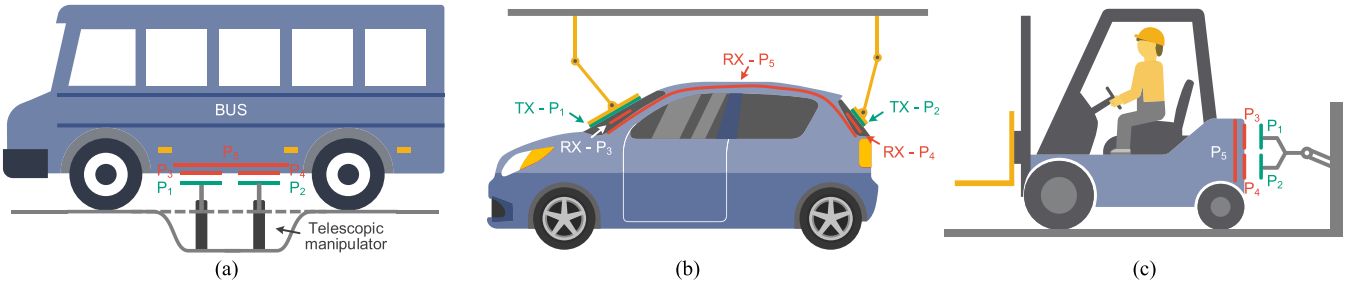

Fig. 29. Some other potential application scenarios for the five-plate coupler. (a) Strongly coupled coupler structure for cars or buses with high chassis. (b) Roof-mounted or window-mounted coupler structure with a mechanical arm on the transmitter side. (c) Coupler structure mounted on the side of a vehicle.

six-plate couplers offer simultaneous shielding on both the transmitter and receiver sides, the five-plate coupler provides a cost-effective, simpler alternative where double-side shielding is not needed. Moreover, it provides a higher coupling coefficient compared to six-plate design, facilitating efficiency improvements. Fig. 4 illustrates a typical shore-to-ship wireless charging scenario utilizing a five-plate coupler, leveraging the expansive shore area and compact receiver side. Fig. 29 presents additional applications.

For electric vehicle wireless charging, traditional methods involve mounting the transmitter plate on the ground and the receiver plate on the chassis. Due to the significant distance between the chassis and the ground, the coupler size must be large to ensure sufficient coupling capacitance. Methods from studies such as [40] suggest using a telescopic manipulator to bring the transmitter side closer to the receiver side during charging, reducing the receiver's volume and weight for easier vehicle integration. This method is particularly suitable for high-chassis electric vehicles, such as electric buses, as shown in Fig. 29(a).

According to Sinha et al. [41], when the coupler is close to both the vehicle chassis and the ground, parasitic effects become significant, forming a six-plate structure. Consequently, vehicles with lower chassis heights may not function as effective as five-plate couplers. However, couplers can be installed in locations such as vehicle windows [42] or bumpers [43] to achieve shorter transfer distances and higher coupling capacitance. Proper shielding on the receiver side allows the five-plate coupler to be used effectively in these cases.

As shown in Fig. 29(b), couplers can be installed on the roof or windows of vehicles. This installation method is also suitable for suspended industrial robots. As illustrated in Fig. 29(c), where couplers are mounted on the back of forklifts. Similar applications can be extended to automated guided vehicles and other automotive contexts.

Appendix B

This appendix provides examples of asymmetric couplers, which can benefit from the efficiency optimization techniques proposed in this study to further enhance performance.

As shown in Fig. 30(a), the receiver side of CPT is typically more compact. In addition, in applications requiring greater tolerance to misalignment, the coupler on one side is often reduced in size, resulting in an asymmetric structure.

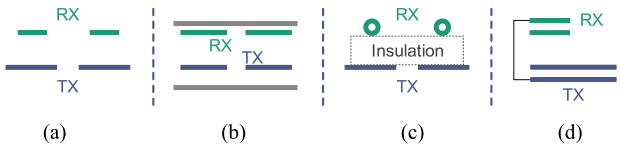

Fig. 30. Some examples of asymmetric couplers. (a) Miniaturization of the receiver side for the purpose of reducing size or improving offset tolerance. (b) Asymmetric six-plate coupler to ensure compactness and passability of a car chassis. (c) Coupler suitable for UAVs. (d) Coupler suitable for dynamic charging of trains.

The same principle applies to six-plate couplers. To ensure compactness and clearance in automotive chassis, the distance between the power transfer plate and the shielding plate on the receiver side is minimized. In contrast, the distance on the transmitter side can be larger. According to the efficiency optimization method, increasing the shielding distance on the transmitter side can improve the coupling coefficient and thus enhance efficiency, as illustrated in Fig. 30(b).

In [44], a CPT coupler is designed for unmanned aerial vehicles (UAVs). Copper foil is wrapped around the UAV's landing gear on the receiver side, while a large plate is employed on the transmitter side. This design effectively improves misalignment tolerance and ensures adequate coupling. The efficiency optimization method proposed in this article can further enhance the performance of this typical asymmetric coupler, as shown in Fig. 30(c).

In [13], a CPT coupler is proposed for dynamic charging of trains. The transmitter side is mounted on the track, while the receiver side is installed on the train. A plate on the receiver side connects to a plate on the transmitter side via the wheels. As a result, the receiver side is smaller than the transmitter side, creating an asymmetric structure. The efficiency optimization method proposed in this article is also applicable to this system, as depicted in Fig. 30(d).

References

[1] J. Mai, A. Yang, Y. Wang, and D. Xu, "Analysis and design of the LC filter rectifier with zero input impedance angle for IPT system," *IEEE Trans. Power Electron.*, vol. 38, no. 12, pp. 14806–14817, Dec. 2023, doi: 10.1109/TPEL.2023.3309637.

[2] R. Xie, R. Liu, X. Chen, X. Mao, X. Li, and Y. Zhang, "An interoperable wireless power transmitter for unipolar and bipolar receiving coils based on three-switch dual-output inverter," *IEEE Trans. Power Electron.*, vol. 39, no. 2, pp. 1985–1989, Feb. 2024, doi: 10.1109/TPEL.2023.3337015.

[3] C. Cai et al., "Optical fiber composite winding for in situ thermal monitoring of transmitter magnetic mechanism in long-track DWPT systems," *IEEE Trans. Instrum. Meas.*, vol. 73, 2024, Art. no. 9000604, doi: 10.1109/TIM.2023.3329107.

[4] E. Rong, P. Sun, K. Qiao, X. Zhang, G. Yang, and X. Wu, "Six-plate and hybrid-dielectric capacitive coupler for underwater wireless power transfer," *IEEE Trans. Power Electron.*, vol. 39, no. 2, pp. 2867–2881, Feb. 2024, doi: 10.1109/TPEL.2023.3334888.

[5] S. Wu, C. Cai, X. Liu, W. Chai, and S. Yang, "Compact and free-positioning omnidirectional wireless power transfer system for unmanned aerial vehicle charging applications," *IEEE Trans. Power Electron.*, vol. 37, no. 8, pp. 8790–8794, Aug. 2022, doi: 10.1109/TPEL.2022.3158610.

[6] Y. Gu, J. Wang, Z. Liang, and Z. Zhang, "A wireless in-flight charging range extended PT-WPT system using s/single-inductor-double-capacitor compensation network for drones," *IEEE Trans. Power Electron.*, vol. 38, no. 10, pp. 11847–11858, Oct. 2023, doi: 10.1109/TPEL.2023.3294485.

[7] T. Li, Z. Sun, Y. Wang, J. Mai, and D. Xu, "Undersea simultaneous wireless power and data transfer system with extended communication distance and high rate," *IEEE Trans. Power Electron.*, vol. 39, no. 3, pp. 2917–2921, Mar. 2024, doi: 10.1109/TPEL.2023.3337801.

[8] Z. Yan et al., "Free-rotation wireless power transfer system based on composite anti-misalignment method for AUVs," *IEEE Trans. Power Electron.*, vol. 38, no. 4, pp. 4262–4266, Apr. 2023, doi: 10.1109/TPEL.2023.3238066.

[9] M. Tamura, T. Segawa, and M. Matsumoto, "Capacitive coupler for wireless power transfer to intravascular implant devices," *IEEE Microw. Wireless Compon. Lett.*, vol. 32, no. 6, pp. 672–675, Jun. 2022, doi: 10.1109/LMWC.2022.3160688.

[10] Z. Liu, T. Li, S. Li, and C. C. Mi, "Advancements and challenges in wireless power transfer: A comprehensive review," *Nexus*, vol. 1, Jun. 2024, Art. no. 100014, doi: 10.1016/j.ynexs.2024.100014.

[11] B. Regensburger, S. Sinha, A. Kumar, S. Maji, and K. K. Afridi, "High-performance multi-MHz capacitive wireless power transfer system for EV charging utilizing interleaved-foil coupled inductors," *IEEE J. Emerg. Sel. Topics Power Electron.*, vol. 10, no. 1, pp. 35–51, Feb. 2022, doi: 10.1109/JESTPE.2020.3030757.

[12] F. Lu, H. Zhang, H. Hofmann, and C. Mi, "A double-sided LCLC-compensated capacitive power transfer system for electric vehicle charging," *IEEE Trans. Power Electron.*, vol. 30, no. 11, pp. 6011–6014, Nov. 2015, doi: 10.1109/TPEL.2015.2446891.

[13] D. C. Ludois, K. J. Frankforter, B. Ge, A. N. Ghule, P. Killeen, and R. P. Knippel, "Macroscale electrostatic rotating machines and drives: A review and multiplicative gain performance strategy," *IEEE J. Emerg. Sel. Topics Power Electron.*, vol. 10, no. 1, pp. 14–34, Feb. 2022, doi: 10.1109/JESTPE.2020.3023118.

[14] S. Li, Z. Liu, H. Zhao, L. Zhu, C. Shuai, and Z. Chen, "Wireless power transfer by electric field resonance and its application in dynamic charging," *IEEE Trans. Ind. Electron.*, vol. 63, no. 10, pp. 6602–6612, Oct. 2016, doi: 10.1109/TIE.2016.2577625.

[15] E. Rong, P. Sun, M. Liu, H. Ji, G. Yang, and X. Wu, "Five-plate coupler for single-side shielding applications in capacitive power transfer," in *Proc. IEEE 7th Int. Elect. Energy Conf.*, 2024, pp. 3492–3497, doi: 10.1109/CIEEC60922.2024.10583238.

[16] F. Lu, H. Zhang, and C. Mi, "A two-plate capacitive wireless power transfer system for electric vehicle charging applications," *IEEE Trans. Power Electron.*, vol. 33, no. 2, pp. 964–969, Feb. 2018, doi: 10.1109/TPEL.2017.2735365.

[17] Z. Liu, Y. Su, H. Hu, Z. Deng, and R. Deng, "Research on transfer mechanism and power improvement technology of the SCC-WPT system," *IEEE Trans. Power Electron.*, vol. 38, no. 1, pp. 1324–1335, Jan. 2023, doi: 10.1109/TPEL.2022.3202074.

[18] J. Lian, X. Qu, X. Chen, and C. C. Mi, "Design of a double-sided LCLC-compensated capacitive power transfer system with predesigned coupler plate voltage stresses," *IEEE J. Emerg. Sel. Topics Power Electron.*, vol. 10, no. 1, pp. 128–137, Feb. 2022, doi: 10.1109/JESTPE.2020.3030657.

[19] T. Chen, C. Cheng, X. Zhang, G. Li, Y. Guo, and C. C. Mi, "A double-sided LCL-compensated network for the strongly coupled CPT system with minimum plate voltage stresses," *IEEE J. Emerg. Sel. Topics Power Electron.*, vol. 12, no. 4, pp. 4275–4287, Aug. 2024, doi: 10.1109/JESTPE.2024.3400874.

[20] H. Zhang, F. Lu, H. Hofmann, W. Liu, and C. C. Mi, "A four-plate compact capacitive coupler design and LCL-compensated topology for capacitive power transfer in electric vehicle charging application," *IEEE Trans. Power Electron.*, vol. 31, no. 12, pp. 8541–8551, Dec. 2016, doi: 10.1109/TPEL.2016.2520963.

[21] W. Zhou, D. Tang, Z. Chen, R. Mai, and Z. He, "Nonisolation model and load virtual-grounding design method for capacitive power transfer system with asymmetric four-plate coupling interface," *IEEE J. Emerg. Sel. Topics Power Electron.*, vol. 12, no. 1, pp. 208–218, Feb. 2024, doi: 10.1109/JESTPE.2023.3312370.

[22] H. Zhang, F. Lu, H. Hofmann, W. Liu, and C. C. Mi, "Six-plate capacitive coupler to reduce electric field emission in large air-gap capacitive power transfer," *IEEE Trans. Power Electron.*, vol. 33, no. 1, pp. 665–675, Jan. 2018, doi: 10.1109/TPEL.2017.2662583.

[23] Y. Liu, T. Wu, and M. Fu, "Interleaved capacitive coupler for wireless power transfer," *IEEE Trans. Power Electron.*, vol. 36, no. 12, pp. 13526–13535, Dec. 2021, doi: 10.1109/TPEL.2021.3086629.

[24] W. Zhou, L. Huang, B. Luo, R. Mai, Z. He, and A. P. Hu, "A general mutual coupling model of MIMO capacitive coupling interface with arbitrary number of ports," *IEEE Trans. Power Electron.*, vol. 36, no. 6, pp. 6163–6167, Jun. 2021, doi: 10.1109/TPEL.2020.3034372.

[25] W. Zhou, Q. Gao, R. Mai, Z. He, and A. P. Hu, "Design and analysis of a CPT system with extendable pairs of electric field couplers," *IEEE Trans. Power Electron.*, vol. 37, no. 6, pp. 7443–7455, Jun. 2022, doi: 10.1109/TPEL.2021.3134708.

[26] T. Chen, C. Cheng, H. Cheng, C. Wang, and C. C. Mi, "Load-independent power-repeater capacitive power transfer system with multiple constant voltage outputs," *IEEE J. Emerg. Sel. Topics Power Electron.*, vol. 10, no. 5, pp. 6358–6370, Oct. 2022, doi: 10.1109/JESTPE.2022.3180029.

[27] H. Zhang, F. Lu, H. Hofmann, W. Liu, and C. C. Mi, "An LC-compensated electric field repeater for long-distance capacitive power transfer," *IEEE Trans. Ind. Appl.*, vol. 53, no. 5, pp. 4914–4922, Sep./Oct. 2017, doi: 10.1109/TIA.2017.2697846.

[28] L. Li, Z. Wang, F. Gao, S. Wang, and J. Deng, "A family of compensation topologies for capacitive power transfer converters for wireless electric vehicle charger," *Appl. Energy*, vol. 260, Feb. 2020, Art. no. 114156, doi: 10.1016/j.apenergy.2019.114156.

[29] Y. Wang, H. Zhang, and F. Lu, "Review, analysis, and design of four basic CPT topologies and the application of high-order compensation networks," *IEEE Trans. Power Electron.*, vol. 37, no. 5, pp. 6181–6193, May 2022, doi: 10.1109/TPEL.2021.3131625.

[30] S. Wang, Y. Yin, R. He, J. Liang, and M. Fu, "High-order compensated capacitive power transfer systems with misalignment insensitive resonance," *IEEE Trans. Circuits Syst. I, Reg. Papers*, vol. 69, no. 8, pp. 3450–3460, Aug. 2022, doi: 10.1109/TCSI.2022.3176896.

[31] S. Wang, J. Liang, and M. Fu, "Analysis and design of capacitive power transfer systems based on induced voltage source model," *IEEE Trans. Power Electron.*, vol. 35, no. 10, pp. 10532–10541, Oct. 2020, doi: 10.1109/TPEL.2020.2981675.

[32] Y. Wu, Q. Chen, X. Ren, and Z. Zhang, "Efficiency optimization based parameter design method for the capacitive power transfer system," *IEEE Trans. Power Electron.*, vol. 36, no. 8, pp. 8774–8785, Aug. 2021, doi: 10.1109/TPEL.2021.3049474.

[33] S. Kodeeswaran, M. N. Gayathri, A. Kannabhiran, and S. S. Williamson, "Design of a static capacitive power transfer system with six-plate coupler for electric vehicle wireless charging," *IEEE Trans. Transport. Electrific.*, vol. 10, no. 2, pp. 3927–3939, Jun. 2024, doi: 10.1109/TTE.2023.3316710.

[34] Y. Wang, H. Zhang, and F. Lu, "3.5-kW 94.2% dc–dc efficiency capacitive power transfer with zero reactive power circulating," *IEEE Trans. Power Electron.*, vol. 38, no. 2, pp. 1479–1484, Feb. 2023, doi: 10.1109/TPEL.2022.3215283.

[35] J. Xia, X. Yuan, S. Lu, J. Li, S. Luo, and S. Li, "A two-stage parameter optimization method for capacitive power transfer systems," *IEEE Trans. Power Electron.*, vol. 37, no. 1, pp. 1102–1117, Jan. 2022, doi: 10.1109/TPEL.2021.3097344.

[36] G. Guidi, J. A. Suul, F. Jenset, and I. Sorfonn, "Wireless charging for ships: High-power inductive charging for battery electric and plug-in hybrid vessels," *IEEE Electrific. Mag.*, vol. 5, no. 3, pp. 22–32, Sep. 2017, doi: 10.1109/MELE.2017.2718829.

[37] C. Yu et al., "Wireless power transfer technology for shore-to-ship applications," in *Proc. Int. Conf. Power Energy Appl.*, 2022, pp. 157–163, doi: 10.1109/ICPEA56363.2022.10052116.

[38] Y. Li, J. Hu, F. Chen, Z. Li, Z. He, and R. Mai, "Dual-phase-shift control scheme with current-stress and efficiency optimization for wireless power transfer systems," *IEEE Trans. Circuits Syst. I, Reg. Papers*, vol. 65, no. 9, pp. 3110–3121, Sep. 2018, doi: 10.1109/TCSI.2018.2817254.

[39] S. Li, S. Lu, and C. C. Mi, "Revolution of electric vehicle charging technologies accelerated by wide bandgap devices," *Proc. IEEE*, vol. 109, no. 6, pp. 985–1003, Jun. 2021, doi: 10.1109/JPROC.2021.3071977.

[40] R. Xie, Y. Wu, H. Tang, Y. Zhuang, and Y. Zhang, "A strongly coupled vehicle-to-vehicle wireless charging system for emergency charging purposes with constant-current and constant-voltage charging capabilities," *IEEE Trans. Power Electron.*, vol. 39, no. 4, pp. 3985–3989, Apr. 2024, doi: 10.1109/TPEL.2024.3352909.

[41] S. Sinha, A. Kumar, B. Regensburger, and K. K. Afridi, "A new design approach to mitigating the effect of parasitics in capacitive wireless power transfer systems for electric vehicle charging," *IEEE Trans. Transport. Electrific.*, vol. 5, no. 4, pp. 1040–1059, Dec. 2019, doi: 10.1109/TTE.2019.2931869.

[42] K. Yi, "Capacitive coupling wireless power transfer with quasi-LLC resonant converter using electric vehicles windows," *Electronics*, vol. 9, no. 4, Apr. 2020, Art. no. 676, doi: 10.3390/electronics9040676.

[43] J. Dai and D. C. Ludois, "Capacitive power transfer through a conformal bumper for electric vehicle charging," *IEEE J. Emerg. Sel. Topics Power Electron.*, vol. 4, no. 3, pp. 1015–1025, Sep. 2016, doi: 10.1109/JESTPE.2015.2505622.

[44] C. Cai, X. Liu, S. Wu, X. Chen, W. Chai, and S. Yang, "A misalignment tolerance and lightweight wireless charging system via reconfigurable capacitive coupling for unmanned aerial vehicle applications," *IEEE Trans. Power Electron.*, vol. 38, no. 1, pp. 22–26, Jan. 2023, doi: 10.1109/TPEL.2022.3198529.

Enguo Rong (Graduate Student Member, IEEE) received the B.S. degree in electrical engineering and the M.S. degree in power electronics from the Kunming University of Science and Technology, Kunming, China, in 2016 and 2019, respectively. He is currently working toward the Ph.D. degree in electrical engineering with the Naval University of Engineering, Wuhan, China.

From 2019 to 2021, he was the CEO of Kunming Minya Technology Company, Ltd., a company focused on the development of high-power converters. His research interests include high-frequency dc–dc converters, magnetic integration, and wireless power transfer systems.

Mr. Rong was the recipient of the Grand Prize Award from the IEEE International Future Energy Challenge in 2017.

Pan Sun received the B.S., M.S., and Ph.D. degrees in electrical engineering from the Naval University of Engineering (NUE), Wuhan, China, in 2009, 2015, and 2022, respectively.

In June 2015, he joined the School of Electrical Engineering, NUE, as an Associate Professor. He authored more than 70 papers with more than 30 being published in SCI and EI journals such as IEEE transactions and other prestigious publications. He successively led the National Key Research and Development Program, the National Natural Science Foundation, and other research projects. His research interests include wireless power transfer, special motors, and their control.

Dr. Sun was a recipient of five provincial and ministerial awards for scientific and technological progress and teaching achievement awards.

Gang Yang received the B.S. and M.S. degrees in electrical engineering in 2014 and 2021, respectively, from the Naval University of Engineering (NUE), Wuhan, China, where he is currently working toward the Ph.D. degree in electrical engineering.

In June 2019, he joined the School of Electrical Engineering, NUE, as a Lecturer. His research interests include capacitive wireless power transfer and the testability of electrical equipment.

Jinglin Xia (Member, IEEE) received the B.S. degree in vehicle operation engineering, the M.E. degree in power engineering, and the Ph.D. degree in power engineering and engineering thermophysics from Jilin University, Changchun, China, in 2015, 2018, and 2022, respectively.

He is currently a Postdoctoral Fellow with the Kunming University of Science and Technology, Kunming, China. His research interests include ac–dc converters, dc–dc converters, and their applications on wireless power transfer.

Zhe Liu (Member, IEEE) received the B.E. degree in electrical engineering from the Chongqing University of Technology, Chongqing, China, in 2014, and the M.E. degree in electrical engineering from the Kunming University of Science and Technology (KUST), Kunming, China, in 2017, and the Ph.D. degree in control theory and control science from Chongqing University, Chongqing, China, in 2023.

Since 2023, he has been with the Faculty of Electric Power Engineering, KUST, where he is currently a Special-Term Associate Professor. His research interests include capacitive power transfer and the single capacitive coupled wireless power transfer.

Siqi Li (Member, IEEE) received the B.S. and Ph.D. degrees in electrical engineering from Tsinghua University, Beijing, China, in 2004 and 2010, respectively.

He was a Postdoctoral Fellow with the University of Michigan, Dearborn, MI, USA, from 2011 to 2013. He was a Visiting Scholar with San Diego State University, San Diego, CA, USA, from 2018 to 2019. In 2013, he joined the Faculty of Electric Power Engineering, Kunming University of Science and Technology (KUST), Kunming, China, where he is currently a Professor with the Department of Electrical Engineering. He is also the Director of the Advanced Power Electronics and New Energy Laboratory, KUST. His research interests include battery management systems, high-performance wired and wireless battery chargers for electric vehicles, and solid-state transformers.